Available online at www.sciencedirect.com
ScienceDirect
Trans. Nonferrous Met. Soc. China 33(2023) 2772−2783
Transactions of Nonferrous Metals Society of China
www.tnmsc.cn

Enhancement of lithium storage performance of $ZnMn_2O_4$ anode by optimizing hydrothermal synthesis

Ke-xing CAI[1,2], Shao-hua LUO[1,2,3], Jun CONG[1,2], Kun LI[1,2], Sheng-xue YAN[1,2], Peng-qing HOU[2,4], Qing WANG[1,2], Ya-hui ZHANG[1,2], Xin LIU[1,2]

1. School of Materials Science and Engineering, Northeastern University, Shenyang 110819, China;
2. Hebei Key Laboratory of Dielectric and Electrolyte Functional Material, School of Resources and Materials, Northeastern University at Qinhuangdao, Qinhuangdao 066004, China;
3. State Key Laboratory of Rolling and Automation, Northeastern University, Shenyang 110819, China;
4. School of Materials Science and Engineering, Shenyang University of Technology, Shenyang 110870, China

Received 19 March 2022; accepted 6 June 2022

Abstract: To explore the effect of the preparation conditions on the electrochemical properties of transition metal oxide anode materials, $ZnMn_2O_4$ anode material was hydrothermally synthesized using zinc nitrate and manganese nitrate as raw materials. The effects of reaction temperature, reaction time, compactness, and pH on the synthesis conditions were systematically studied through an orthogonal test designed with four factors and three levels. X-ray diffraction and scanning electron microscopy proved the formation of a micron-scale block-like $ZnMn_2O_4$ structure with the $I4_1/amd$ space group. The Li/$ZnMn_2O_4$ cells delivered an initial discharge specific capacity of 933.1 mA·h/g, and the discharge specific capacity remained at 249.3 mA·h/g after 100 cycles at a current rate of 0.1C for the as-synthesized $ZnMn_2O_4$ under the optimized conditions. The optimized sample with orthogonal test exhibits outstanding cycle stability and rate performance.

Key words: spinel $ZnMn_2O_4$ structure; lithium-ion battery; electrochemical performance; hydrothermal reaction; orthogonal test

1 Introduction

The overexploitation of fossil fuels has exacerbated the energy crisis, necessitating the emergence of a new energy industry [1−4]. Energy storage devices are significant in this new energy industry, and lithium-ion batteries play a leading role in the energy storage device industry [5−7]. One of the key components of a lithium-ion battery is the anode material, which significantly impacts the overall performance of the battery. Graphite anode materials lack sufficient capacity to meet the increasing power and energy density demands of modern society because they have a solid electrolyte interface, low lithium intercalation voltage, and significant charge loss. Therefore, the demand for high-capacity lithium-ion batteries has stimulated the investigation of other types of anode materials [8−12].

Recently, transition metal oxides have become a research hotspot due to their highly reversible reactions and stable structure in the battery's electrochemical window [13,14]. These transition metal oxides, especially Fe, Zn, Mn, Co, Ni, and Cu, can undergo a reversible reaction with lithium: $M_xO_y+2ye+2yLi^+ \rightleftharpoons xM^0+yLi_2O$. This electrode reaction forms a composite material with metal particles distributed on an amorphous Li_2O substrate. In 2000, POIZOT et al [15] discovered

Corresponding author: Shao-hua LUO, Tel: +86-335-8047760, E-mail: tianyanglsh@163.com
DOI: 10.1016/S1003-6326(23)66297-1

that transition metal oxides can undergo a reversible electrochemical reaction with lithium metal. Among them, zinc manganate ($ZnMn_2O_4$) has attracted significant attention because it offers environmental protection, low cost, and a low working potential. This material has a high melting point, hardness, and chemical stability due to its strong bond energy. $ZnMn_2O_4$ with a three-dimensional network channel can undergo Zn^0 and Mn^0 conversion reactions at low potentials. Concurrently, lithium metal can form an alloy with Zn at low potentials, affording a high lithium storage capacity. After integration into a battery, the potential and energy density of lithium are improved owing to the high lithium storage and low discharge platforms in lithium batteries [16]. However, as a special binary transition metal oxide, $ZnMn_2O_4$ faces several challenges in its preparation process. For example, after high-temperature annealing, the material's structure and morphology are difficult to control and agglomeration is common [17−19]. Therefore, improving the zinc manganate synthesis method and electrochemical performance is worthwhile.

Currently, $ZnMn_2O_4$ is prepared using the sol–gel method [20], the coprecipitation method [21], the template method [22], electrospinning [23], and various other methods. Although these methods have their own advantages, they need high-temperature calcination to synthesize $ZnMn_2O_4$ materials. The low-temperature hydrothermal method is a lower-cost and more advanced method for synthesizing $ZnMn_2O_4$ powder than traditional methods [24−26]. Herein, we designed orthogonal experiments to explore the optimal conditions for the hydrothermal synthesis of $ZnMn_2O_4$ using zinc nitrate and manganese nitrate as raw materials. The spinel $ZnMn_2O_4$ material synthesized using the hydrothermal method has high thermal stability, small particle size, and uniform distribution. The electrochemical properties of the samples synthesized under the optimum conditions were analyzed using several test methods, and the electrochemical reaction mechanism was explored. $ZnMn_2O_4$ delivered a high initial discharge specific capacity of 933.1 mA·h/g at a current rate of 0.1C (1C=1008 mA·h/g). After 100 cycles, the specific capacity remained at 249.3 mA·h/g. This research is expected to provide a theoretical and experimental basis for the research of transition metal oxide anode materials.

2 Experimental

2.1 Material preparation

Figure 1 shows the synthesis path of $ZnMn_2O_4$ via the hydrothermal method. Zinc nitrate and manganese nitrate were added at a stoichiometric ratio into a beaker and dissolved in deionized water. The compactness and pH were adjusted to a set of values displayed in the orthogonal table (Table 1) and the mixture was poured into a Teflon-lined stainless-steel autoclave. The autoclave was sealed and placed in a homogeneous reactor. After setting the reaction temperature and running the reaction for a certain time, the autoclave was removed and the precipitates were filtered and washed twice to obtain $ZnMn_2O_4$ materials synthesized under different conditions.

Fig. 1 Flow chart of $ZnMn_2O_4$ material prepared by low-temperature hydrothermal method

Table 1 Factor−level table $L_9(3^4)$ designed for synthesizing $ZnMn_2O_4$ material using hydrothermal method

Level	Factor			
	Reaction temperature/°C	Reaction time/d	Compactness/ vol.%	pH
1	180	1	73	3
2	200	2	80	7
3	220	3	87	11

2.2 Material characterization

The phase compositions and crystal structures of the samples were investigated using X-ray diffraction (XRD, DX−2500, Cu K_α radiation), and the 2θ range was 10°−80°. The geometric morphology, particle morphology, and size information were investigated using a scanning

electron microscope (SEM, S−4800). The elemental distribution was investigated using energy dispersive X-ray spectroscopy. The pore size distribution and specific surface area of the samples were analyzed using the N_2 adsorption–desorption method.

2.3 Electrochemical measurements

The electrode slurry was prepared by mixing the active material, acetylene black, and PVDF binder in the mass ratio of 8:1:1 with N-methyl pyrrolidone (NMP) as the solvent. The mixed slurry was uniformly adhered to the copper foil, dried under vacuum at 120 °C, and cut into 10 mm diameter electrodes. Further, the cut electrode pieces were weighed, the mass of each electrode piece was recorded, and the mass of active substances was calculated. Subsequently, the CR2032 half-cell in a glove box filled with argon was assembled and kept at room temperature for one night to be tested. The battery test system (LAND, CT−2001A) was used to test the charge− discharge specific capacity, cycle life, and capacity retention of anode materials in the potential range of 0−3 V at various charge–discharge rates and 25 °C. A cyclic voltammetry test was conducted on the CHI660A electrochemical workstation. The electrochemical impedance spectroscopy (EIS) was conducted on the CHI760E electrochemical workstation, and the test frequency range was 10^{-2}−10^{5} Hz.

3 Results and discussion

3.1 Characterization results of $ZnMn_2O_4$

Figure 2 shows the XRD patterns of nine groups of $ZnMn_2O_4$ samples under different experimental conditions. Different experimental conditions significantly impact phase compositions of the samples. From the relative intensity of the peak, the samples synthesized using a low-temperature hydrothermal process have good crystallinity. In terms of phase composition, the main peaks of S1, S6, and S8 samples accurately correspond to the PDF standard card of Mn_2O_3 (JCPDS No. 41-1442, space group *Ia*-3, and $a=b=c=9.409$ Å), indicating that the Mn_2O_3 phase is generated in an acidic preparation environment (pH=3) [27]. The spinel $ZnMn_2O_4$ structure obtained from S2, S3, S4, S5, S7, and S9 samples correspond to the PDF standard card (JCPDS No. 24-1133, space group $I4_1/amd$, $a=b=5.72$ Å, and

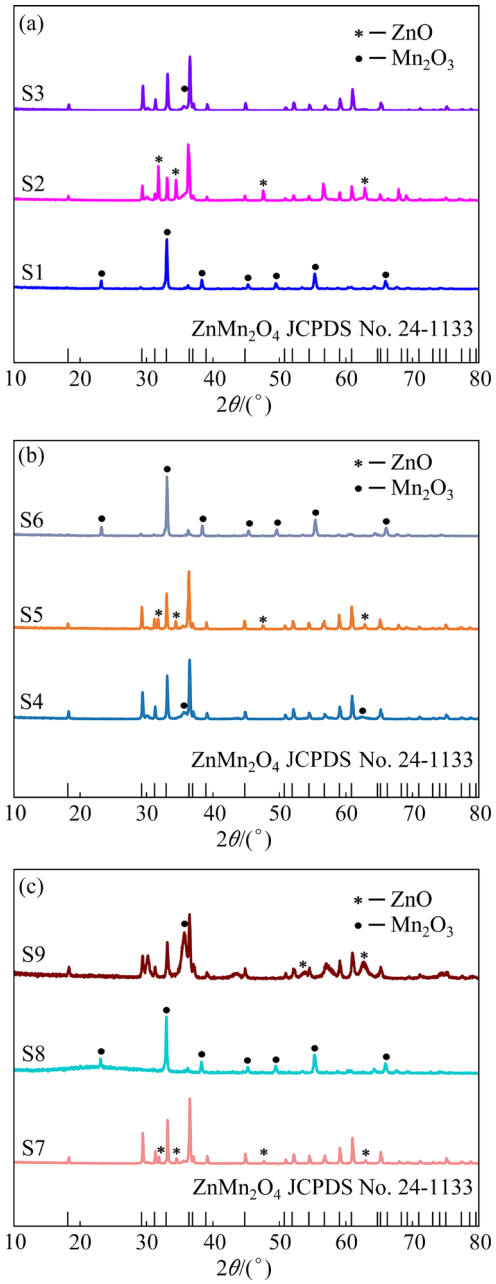

Fig. 2 XRD patterns of nine $ZnMn_2O_4$ samples prepared by hydrothermal method at different temperatures: (a) 180 ℃; (b) 200 ℃; (c) 220 ℃

$c=9.245$ Å). The purity of the $ZnMn_2O_4$ phases synthesized under the six synthesis conditions also varies. Some $ZnMn_2O_4$ samples contain the ZnO impurity phase, which is consistent with the PDF standard card (JCPDS No. 99-0111, space group $P6_3mc$, $a=b=3.25$ Å, and $c=5.207$ Å). Therefore, the hydrothermal preparation of $ZnMn_2O_4$ places strict requirements on the synthesis conditions, and the reaction temperature and time, metal ion concentration, and pH should be controlled.

The mesoporous structure, pore diameter, and specific surface area of the S5 sample were investigated. The nitrogen (N_2) adsorption–desorption isothermal curve and pore size distribution of the $ZnMn_2O_4$ sample were drawn based on the test data (Fig. 3(a)). The adsorption isotherms are divided into six types according to the different shapes. The isothermal curve of the $ZnMn_2O_4$ sample belongs to type IV adsorption isotherm [28,29]. Figure 3(a) shows that the $ZnMn_2O_4$ sample has an obvious hysteresis phenomenon and forms a hysteresis ring. This indicates that there are micropores with pore diameters less than 2 nm and mesopores with pore diameters of 2−50 nm in the sample. The specific surface area of the $ZnMn_2O_4$ sample is 13.824 m^2/g and the pore volume is 0.137 cm^3/g obtained using the BET calculation model. The average pore diameter of the $ZnMn_2O_4$ sample is 38.76 nm obtained using the BJH calculation model. According to the pore size distribution curve (the insert map in Fig. 3(a)), the pore size of the $ZnMn_2O_4$ sample is mainly distributed between 4.5 and 68 nm. Only a few pore size distributions are less than 4.5 nm. The mesoporous structure is the main structure [30]. Alternatively, the mesoporous structure of the anode material can ensure the mechanical strength of the material. Concurrently, the large pores can buffer the volume expansion and contraction of the material in the charge and discharge processes. This structure can prevent structural collapse and material deactivation. Moreover, the mesoporous structure allows the electrolyte penetration, and complete contact between the electrode material and the electrolyte allows for improved discharge specific capacity. In addition, the mesoporous structure provides more paths for the intercalation and deintercalation of Li^+. This structure shortens the transmission distance and improves the reaction rate [31,32]. Figure 3(b) shows the Fourier transform infrared spectrum of S5 sample for further characterization. The peaks in the wavenumber range of 420−640 cm^{-1} are the vibration peaks of M—O—M and M—O (M=Zn and Mn) bonds. The absorption peak observed at 3457 cm^{-1} is due to the stretching vibration of the O—H group of the water molecule in air, and the absorption peak at 1639 cm^{-1} is the vibration peak of the C═O bond of CO_2 in air [33,34].

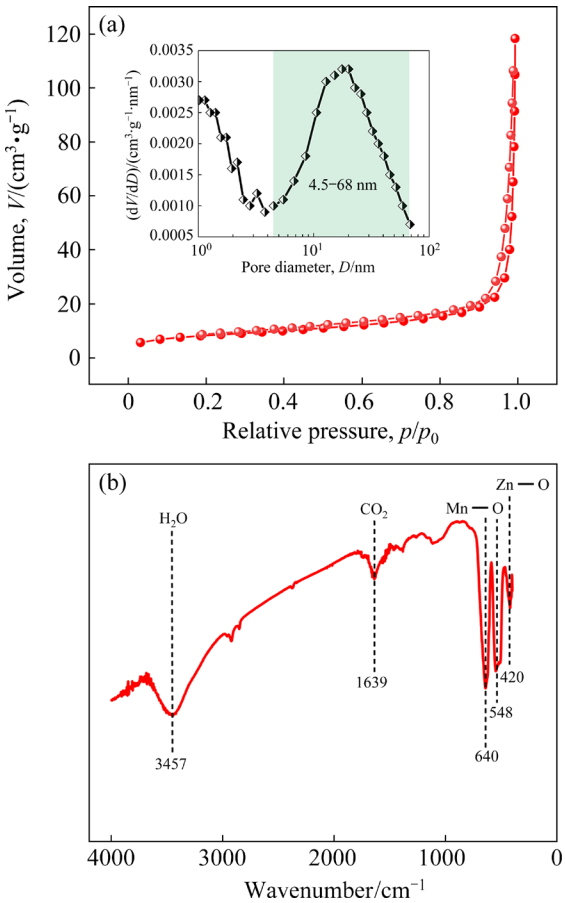

Fig. 3 Diagrams of N_2 adsorption−desorption isotherm and pore size distribution (a), and Fourier transform infrared spectrum (b) of S5 sample

Figures 4(a, b) show the SEM images of $ZnMn_2O_4$ material synthesized by the hydrothermal method. Its morphology is irregular with highly agglomerated small particles. The partially enlarged image shows that these small particles are interwoven by multiple flocculent crystals, indicating a porous structure. This porous structure can promote ion transfer and adapt to the volume expansion and contraction of materials in the electrochemical process [35,36]. From the histogram of the $ZnMn_2O_4$ material's particle size distribution in Fig. 4(c), the size is mainly distributed between 0.5 and 1.7 μm, and the average particle size is 0.90 μm. Employing small-sized $ZnMn_2O_4$ particles as the anode material for lithium-ion batteries increases the active material usage and significantly reduces the diffusion distance of lithium ions [37]. Figure 4(d) shows the elemental surface distribution diagram of the $ZnMn_2O_4$ sample, demonstrating the uniform distribution of Zn, Mn, and O on the surface of the particles.

3.2 Orthogonal experiment results

Using the average discharge specific capacity of 21−40 cycles as the investigation index, the electrochemical properties of $ZnMn_2O_4$ obtained under different synthesis conditions were obtained via range analysis (Table 2). Because only S2, S3, S4, S5, S7, and S9 groups of experiments can be used to successfully synthesize $ZnMn_2O_4$ materials and the main phase of other samples was Mn_2O_3, only the electrochemical properties of six groups of materials with phase compositions of $ZnMn_2O_4$ were tested. As evidenced in Table 2, the average discharge specific capacities of Samples S2, S5, S7, and S9 exceeded 200 mA·h/g. All of these samples contain the ZnO phase. Integrated heterostructure electrode materials composed of different metal

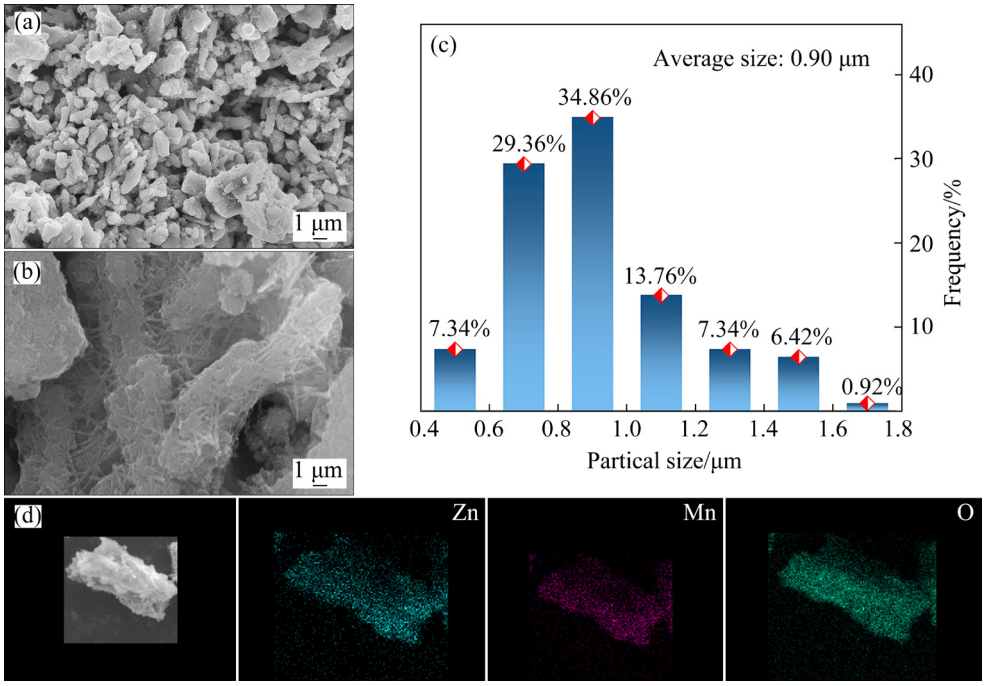

Fig. 4 SEM images (a, b) particle size distribution (c), and EDS mapping (d) of $ZnMn_2O_4$ sample

Table 2 Electrochemical properties of $ZnMn_2O_4$ samples synthesized under different conditions

Sample	Factor				Average specific capacity/(mA·h·g^{-1})
	Reaction temperature/℃	Reaction time/d	Compactness/vol.%	pH	
S1	180	1	73	3	–
S2	180	2	80	7	260.530
S3	180	3	87	11	193.125
S4	200	1	87	7	172.055
S5	200	2	73	11	292.530
S6	200	3	80	3	–
S7	220	1	80	11	206.415
S8	220	2	87	3	–
S9	220	3	73	7	223.125
K_1/(mA·h·g^{-1})	453.655	378.270	515.655	–	
K_2/(mA·h·g^{-1})	464.585	553.060	466.945	655.71	
K_3/(mA·h·g^{-1})	429.540	416.250	365.180	692.07	
R/(mA·h·g^{-1})	35.045	174.790	150.475	36.36	

oxides with different band gap energies can improve the internal electric field at the heterogeneous interface, thereby improving the surface reaction kinetics and charge transfer, and consequently the electrochemical activity [38−41]. Therefore, the composites of ZnO and mixed zinc-based oxides are potential electrode materials, with ZnO contributing positively to the electrochemical properties of the $ZnMn_2O_4$ materials. At pH 3, the phase composition of the synthesized sample is Mn_2O_3. Therefore, the data at pH 3 were excluded from the influence trend of various factors on the $ZnMn_2O_4$ discharge specific capacity in Fig. 5. The reaction time most significantly influences the formation of the $ZnMn_2O_4$ phase, followed by the compactness and pH, and finally the reaction temperature. The optimum conditions for synthesizing $ZnMn_2O_4$ are as follows: reaction temperature 200 °C, reaction time 2 d, compactness 73 vol.%, and pH 11. These optimum conditions were the synthesis conditions of the S5 sample.

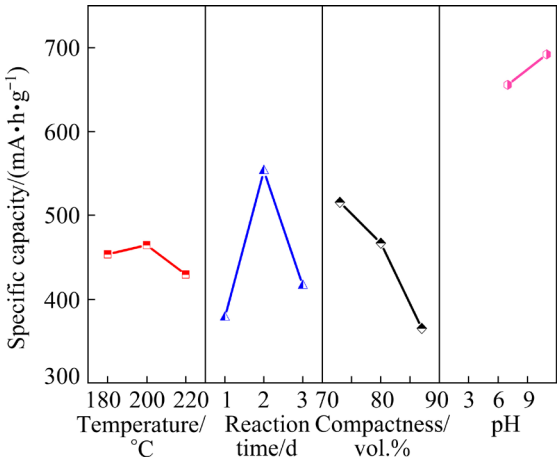

Fig. 5 Diagram showing influence of various factors on discharge specific capacity

3.3 Electrochemical performance of $ZnMn_2O_4$

Figure 6 shows the charge–discharge curves of $ZnMn_2O_4$ synthesized under the six conditions at a 0.1*C* rate (1*C*=1008 mA·h/g). The first discharge specific capacities of the S2, S3, S4, S5, S7, and S9 electrodes are 947.1, 650.2, 781.5, 933.2, 929.3, and 921 mA·h/g, respectively. After the first cycle, the discharge specific capacities of the six electrodes decrease to 570.1, 403.3, 458.7, 509.4, 441.5, and 401.4 mA·h/g, respectively. This capacity loss is mainly caused by electrolyte decomposition and the formation of an SEI membrane [42]. The figure shows that the first cycle discharge platform of the six electrode materials appears between 0.25 and 0.5 V, and the charging platform appears between 1.2 and 1.5 V. The platform gradually decreases and the polarization intensifies as the number of cycles increases [43,44]. The S2 electrode exhibits the highest first discharge performance. However, comparing the average discharge specific capacities (359.1, 292.4, 259.3, and 371.9 mA·h/g) of the six electrodes in the second, fifth, tenth, and twentieth cycles, the S5 electrode exhibits the best cycle performance. This conclusion can also be drawn from Table 2.

The optimization of the synthesis conditions makes $ZnMn_2O_4$ show excellent electrochemical lithium storage performance. We can see the excellent electrochemical performance of the S5 electrode by comparing $ZnMn_2O_4$ materials synthesized under different conditions. Figure 7(a) shows the rate performance of the electrode material at (0.1−1.0)*C* rate in the potential range of 0−3 V (vs Li/Li^+). The average discharge specific capacities of the S5 electrode at 0.1*C*, 0.2*C*, 0.5*C*, and 1*C* are 354.6, 218.1, 147.2, and 105.0 mA·h/g, respectively, which is better than other electrodes. Figure 7(b) shows the cyclic performance of the six groups of electrodes. The coulombic efficiency of the first cycle of all electrodes is around 50%. The coulombic efficiency of the second cycle can be increased to about 80% after the irreversible capacity loss of the first cycle. The irreversible capacity is mainly related to the irreversible redox reaction of Mn^{3+}/Mn^{2+} and the formation of SEI film [45]. In the later cycles, the coulombic efficiency of the S5 electrode exceeds 95%, indicating its excellent capacity retention rate. The discharge specific capacity of each electrode is gradually stabilized after 20 cycles. After 100 cycles, the discharge specific capacity of the S5 electrode remains at 249.3 mA·h/g, exceeding those of the other electrode materials and indicating that the S5 electrode has excellent capacity retention. Comparing the electrochemical performances of the electrodes, the S5 electrode exhibits higher cyclic performance than the other electrodes.

We believe that $ZnMn_2O_4$ has excellent rate performance and cycle stability based on the aforementioned analysis results. Figure 7(c) shows the discharge curve of the first cycle. The S5 electrode has a low discharge platform (0.39 V),

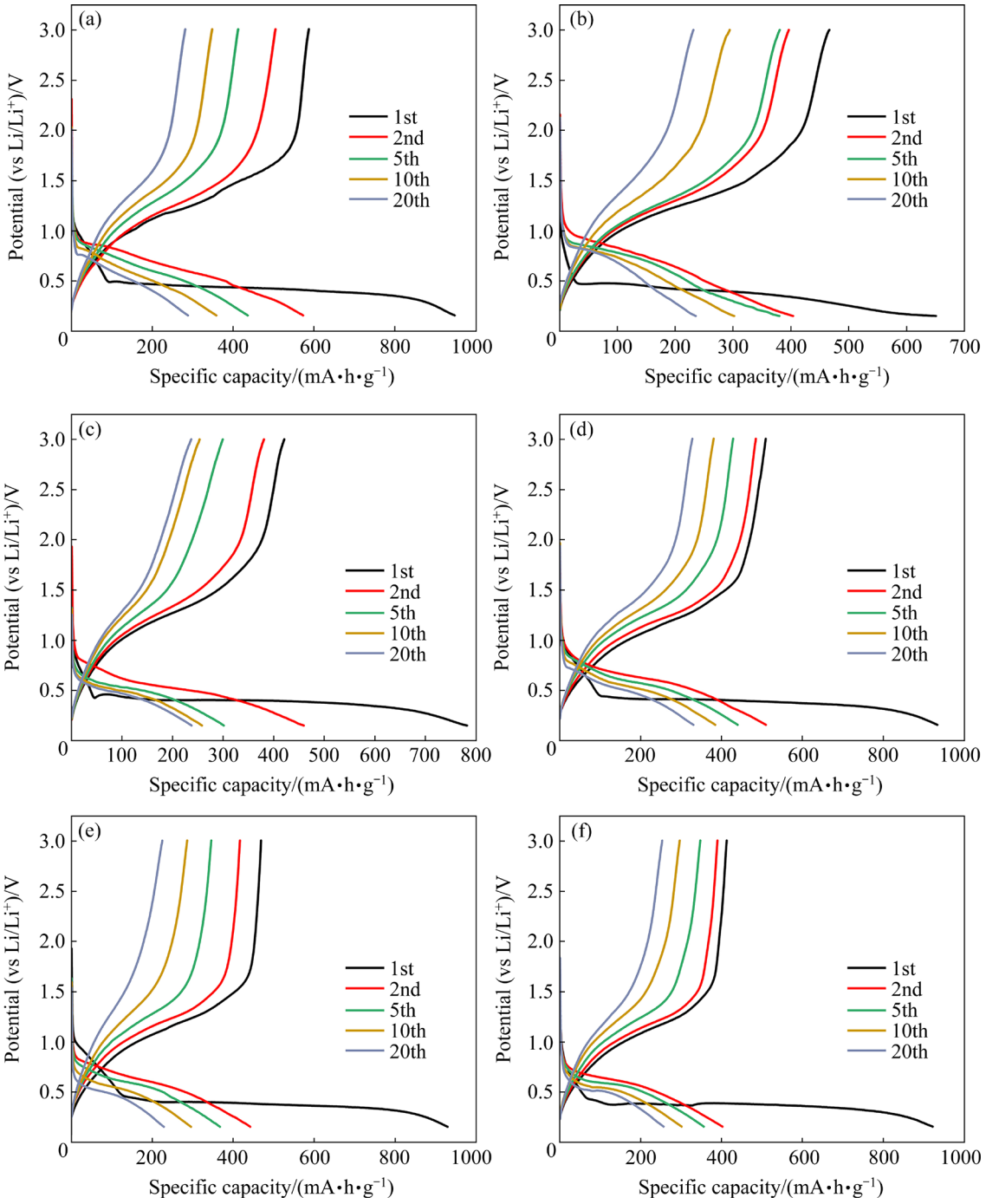

Fig. 6 Discharge−charge potential profiles of $ZnMn_2O_4$ anode under different preparation conditions at 0.1*C* rate: (a) S2; (b) S3; (c) S4; (d) S5; (e) S7; (f) S9

which allows the battery to output a higher voltage and has a higher energy density [46]. Concurrently, we conducted a CV test on the S5 electrode, and the first cycle results are shown in Fig. 7(d). In the first scanning round, the reduction peak at 0.40 V corresponds to the formation of elemental metals, Zn and Mn. Further, the alloying reaction of ZnLi, which is a lithium intercalation process, occurs at this potential. During the oxidation reaction, the oxidation peak at 1.25 V corresponds to the oxidation of Zn and Mn to form Zn^{2+} and Mn^{2+}, dealloying process, and decomposition of Li_2O, which is a lithium deintercalation process [22,47]. Figure 7(e) shows the second cycle charge–discharge curve of the S5 electrode, and its dQ/dφ curve is shown in Fig. 7(f). In the second cycle, the

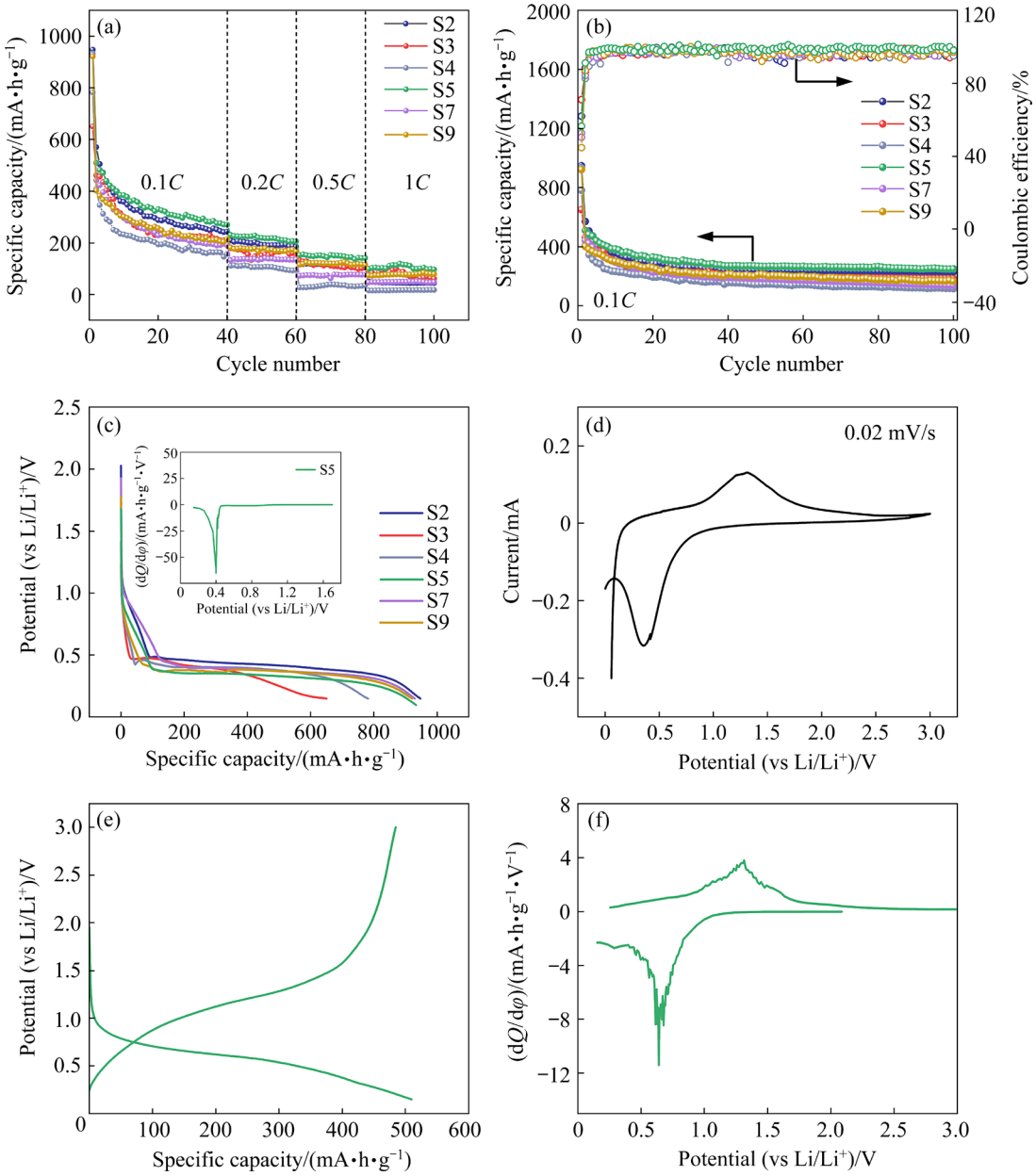

Fig. 7 Rate performance diagram at (0.1−1.0)*C* (a), cyclic performance diagram at 0.1*C* (b) of six ZMO materials, the first cycle discharge curves of six materials (the inset shows the first cycle discharge d*Q*/dφ curve of S5 sample, *Q* is specific capacity of electrode and φ is potential of electrode) (c), first cycle CV curve of S5 sample at scanning rate of 0.02 mV/s (d), second cycle charge−discharge curve (e) and d*Q*/dφ curve (f) of S5 sample

reduction peak corresponding to Zn and Mn moves from 0.40 to 0.61 V, and the oxidation peak of Zn and Mn moves from 1.25 to 1.34 V, which is mainly caused by the structural rearrangement of electrode active materials during the charge−discharge process [48,49]. The material's reaction mechanism is summarized as follows. The first discharge reaction is shown in Reaction (1), which is an irreversible reaction. The theoretical specific capacity calculated from this reaction is 1008 mA·h/g. The subsequent charge–discharge reaction is shown in Reaction (2), and the theoretical specific capacity is 784 mA·h/g, which is a reversible reaction.

$$ZnMn_2O_4+9Li^++9e \rightleftharpoons ZnLi+2Mn+4Li_2O \quad (1)$$

$$ZnLi+2Mn+3Li_2O \rightleftharpoons ZnO+2MnO+7Li^++7e \quad (2)$$

The impedance test of the S5 electrode was conducted to further characterize the material's lithium storage performance (Fig. 8). R_{st} and R_{sf} represent the resistance of the cell components and interfacial film. CPE_{sf} is the SEI capacitance. The

semicircle in the intermediate frequency area is correlated with the charge transfer impedance (R_{ct}) and double-layer capacitance (CPE_{ct}), which is attributed to the charge transfer across the electrode–electrolyte interface and is also the main internal resistance in the lithium-ion battery system. The size of its semicircle can qualitatively represent the size of the impedance value. The smaller the value, the easier it is for Li^+ to intercalate and deintercalate in the material. The reduction in the low-frequency region indicates the transmission capacity of lithium ions in the electrolyte [50,51]. The impedance value of each electrode material was fitted through the equivalent circuit. The R_s values of S2, S3, S4, S5, S7, and S9 electrodes are approximately 3 Ω, indicating consistent conditions of the battery assembly. The charge transfer resistance of the S5 electrode was determined to be 65.3 Ω. Therefore, after optimizing the preparation conditions, the electrochemical reaction resistance of the electrode material was effectively reduced and the electro- chemical activity was improved.

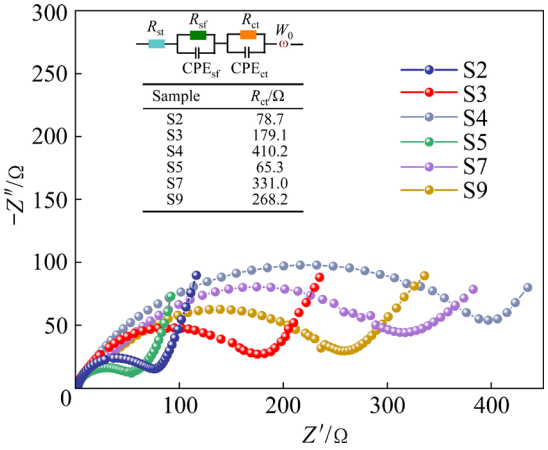

Fig. 8 Electrochemical impedance diagram of different electrodes

4 Conclusions

(1) $ZnMn_2O_4$ material was synthesized using the low-temperature hydrothermal method. Its lithium storage performance was optimized by adjusting the reaction temperature and time, compactness, and pH.

(2) pH significantly affects $ZnMn_2O_4$ synthesis. $ZnMn_2O_4$ is difficult to form under acidic conditions; however, it can be successfully synthesized under neutral or alkaline conditions.

(3) The $ZnMn_2O_4$ synthesis was optimized at a reaction temperature of 200 °C, a reaction time of 2 d, 73 vol.% compactness of the mixed solution, and a pH of 11.

(4) The first discharge specific capacity reached 933.1 mA·h/g at a 0.1*C* rate. The specific capacity remained at 249.3 mA·h/g after 100 cycles. Even at a higher rate (1*C*), the discharge specific capacity remained stable and exceeded 100 mA·h/g.

(5) The electrochemical properties and reaction mechanisms of different electrode materials were investigated in detail using several electrochemical test methods. The study of electrochemical charge–discharge, CV, dQ/dφ, and EIS curves shows that $ZnMn_2O_4$ synthesized under the optimum synthesis conditions exhibits better kinetic properties.

Acknowledgments

The authors are grateful for the financial supports from the National Natural Science Foundation of China (Nos. 51874079, 51674068, 51804035), the Natural Science Foundation of Hebei Province, China (Nos. E2018501091, E2021501029), Hebei Province Key Research and Development Plan Project, China (No. 19211302D), the Fundamental Research Funds for the Central Universities, China (Nos. N172302001, N182312007, N182306001, N2023040), and the Research Project on the Distribution of Heavy Metals in Soil and Comprehensive Utilization Technology of Tailings in Typical Iron Tailing Reservoir Areas of Hebei Province, China (No. 802060671901).

References

[1] TAO Yan-qiu, RAHN C D, ARCHER L A, YOU Feng-qi. Second life and recycling: Energy and environmental sustainability perspectives for high-performance lithium-ion batteries [J]. Science Advances, 2021, 7: eabi7633.

[2] ZHAN Jing, XU Chang-fan, LONG Yi-yu, LI Qi-hou. Preparation and electrochemical performance of nitrogen-doped carbon-coated $Bi_2Mn_4O_{10}$ anode materials for lithium-ion batteries [J]. Transactions of Nonferrous Metals Society of China, 2020, 30: 2188−2199.

[3] QIN Mu-lan, YIN Chang-yu, XU Wen, LIU Yang, WEN Jun-hao, SHEN Bin, WANG Wei-gang, LIU Wan-min. Facile synthesis of high capacity P2-type $Na_{2/3}Fe_{1/2}Mn_{1/2}O_2$ cathode material for sodium-ion batteries [J]. Transactions of Nonferrous Metals Society of China, 2021, 31: 2074−2080.

[4] QIN Mu-lan, LIU Wan-min, XIANG Yuan-jin, WANG Wei-gang, SHEN Bin. Synthesis and electrochemical performance of V_2O_5/NaV_6O_{15} nanocomposites as cathode

materials for sodium-ion batteries [J]. Transactions of Nonferrous Metals Society of China, 2020, 30: 2200−2206.

[5] LI Fang-cheng, ZHANG Gang, ZHANG Zong-liang, YANG Jian, LIU Fang-yang, JIA Ming, JIANG Liang-xing. Regeneration of Al-doped $LiNi_{0.5}Co_{0.2}Mn_{0.3}O_2$ cathode material by simulated hydrometallurgy leachate of spent lithium-ion batteries [J]. Transactions of Nonferrous Metals Society of China, 2022, 32: 593−603.

[6] WANG Qi, LAI Yan-qing, LIU Fang-yang, JIANG Liang-xing, JIA Ming, WANG Xi-lun. Sb_2S_3 nanorods/porous-carbon composite from natural stibnite ore as high-performance anode for lithium-ion batteries [J]. Transactions of Nonferrous Metals Society of China, 2021, 31: 2051−2061.

[7] YANG Jian, JIANG Liang-xing, LIU Fang-yang, JIA Ming, LAI Yan-qing. Reductive acid leaching of valuable metals from spent lithium-ion batteries using hydrazine sulfate as reductant [J]. Transactions of Nonferrous Metals Society of China, 2020, 30: 2256−2264.

[8] JIN Yan, ZHU Bin, LU Zhen-da, LIU Nian, ZHU Jia. Challenges and recent progress in the development of Si anodes for lithium-ion battery [J]. Advanced Energy Materials, 2017, 7: 1700715.

[9] LUO Jing-jing, ZHOU Jian-bin, LIN Dan, REN Yi, TANG Kai-bin. LiFeP: A new anode material for lithium ion batteries [J]. Journal of Power Sources, 2017, 370: 14−19.

[10] MU Tian-sheng, ZUO Peng-jian, LOU Shuai-feng, PAN Qing-rui, LI Qin, DU Chun-yu, GAO Yun-zhi, CHENG Xin-qun, MA Yu-lin, YIN Ge-ping. A two-dimensional nitrogen-rich carbon/silicon composite as high performance anode material for lithium ion batteries [J]. Chemical Engineering Journal, 2018, 341: 37−46.

[11] ZENG Jing, PENG Chao-qun, WANG Ri-chu, LIU Ya-jing, WANG Xiao-feng, LIU Jun. Preparation of dual-shell Si/TiO_2/CFs composite and its lithium storage performance [J]. Transactions of Nonferrous Metals Society of China, 2019, 29: 2384−2391.

[12] LI Lie-wu, WANG Li-ping, ZHANG Ming-yu, HUANG Qi-zhong, HE Ke-jian, WU Fei-xiang. Enhancement of lithium storage capacity and rate performance of Se-modified MnO/Mn_3O_4 hybrid anode material via pseudocapacitive behavior [J]. Transactions of Nonferrous Metals Society of China, 2020, 30: 1904−1915.

[13] ZHAO Yang, LI Xi-fei, YAN Bo, XIONG Dong-bin, LI De-jun, LAWES S, SUN Xue-liang. Recent developments and understanding of novel mixed transition-metal oxides as anodes in lithium ion batteries [J]. Advanced Energy Materials, 2016, 6: 1502175.

[14] ZHENG Ming-bo, TANG Hao, LI Lu-lu, HU Qin, ZHANG Li, XUE Huai-guo, PANG Huan. Hierarchically nanostructured transition metal oxides for lithium-ion batteries [J]. Advanced Science, 2018, 5: 1700592.

[15] POIZOT P, LARUELLE S, GRUGEON S, DUPONT L, TARASCON J M. Nano-sized transition-metal oxides as negative-electrode materials for lithium-ion batteries [J]. Nature, 2000, 407: 496−499.

[16] ZHANG Gen-qiang, YU Le, WU Hao-bin, HOSTER H E, LOU Xiong-wen. Formation of $ZnMn_2O_4$ ball-in-ball hollow microspheres as a high-performance anode for lithium-ion batteries [J]. Advanced Materials, 2012, 24: 4609−4613.

[17] ZHONG Ming, YANG Dong-hui, XIE Chen-chao, ZHANG Zhang, ZHOU Zhen, BU Xian-he. Yolk-shell $MnO@ZnMn_2O_4$/N-C nanorods derived from α-MnO_2/ZIF-8 as anode materials for lithium ion batteries [J]. Small, 2016, 12: 5564−5571.

[18] YIN Long-wei, ZHANG Zhi-wei, LI Zhao-qiang, HAO Feng-bin, LI-Qun, WANG Cheng-xiang, FAN Run-hua, QI Yong-xin. Spinel $ZnMn_2O_4$ nanocrystal-anchored 3D hierarchical carbon aerogel hybrids as anode materials for lithium ion batteries [J]. Advanced Functional Materials, 2014, 24: 4176−4185.

[19] ZHANG Tong, LIANG Hao, XIE Chen-di, QIU Hai-long, FANG Zhi-bo, WANG Lei, YUE Hui-juan, CHEN Gang, WEI Ying-jin, WANG Chun-zhong, ZHANG Dong. Morphology-controllable synthesis of spinel zinc manganate with highly reversible capability for lithium ion battery [J]. Chemical Engineering Journal, 2017, 326: 820−830.

[20] HASAN M, ZAWAR S, MUSTAFA G M, GHAFFAR A, RAZAQ A, ATIQ S. Porous architecture of Ni substituted $ZnMn_2O_4$ nanospheres as an electrode material for supercapacitor applications [J]. Physica B: Condensed Matter, 2022, 633: 413767.

[21] ZHANG Tong, GAO Yu, YUE Hui-juan, QIU Hai-long, GUO Zhen-dong, WEI Ying-jin, WANG Chun-zhong, CHEN Gang, ZHANG Dong. Convenient and high-yielding strategy for preparing nano-$ZnMn_2O_4$ as anode material in lithium-ion batteries [J]. Electrochimica Acta, 2016, 198: 84−90.

[22] ZHANG Li-xin, WANG Ya-lei, JIU Hong-fang, QIU Hao-yang, WANG Hong-yu. Hollow core–shell $ZnMn_2O_4$ microspheres as a high-performance anode material for lithium-ion batteries [J]. Ceramics International, 2015, 41: 9655−9661.

[23] SHAMITHA C, SENTHIL T, WU Li-xin, KUMAR B S, ANANDHAN S. Sol–gel electrospun mesoporous $ZnMn_2O_4$ nanofibers with superior specific surface area [J]. Journal of Materials Science: Materials in Electronics, 2017, 28: 15846−15860.

[24] TOOZANDEHJANI M, OSTOVAN F, JAMALUDIN K R, AMRIN A, MATORI K A. Process−microstructure−properties relationship in Al−CNTs−Al_2O_3 nanocomposites manufactured by hybrid powder metallurgy and microwave sintering process [J]. Transactions of Nonferrous Metals Society of China, 2020, 30: 2339−2354.

[25] DONG Qiu-chun, YANG Jun, WU Mei-yan, ZHOU Xiao, ZHANG Yi-zhou, WANG Wen-jun, SI Wei-li, HUANG Wei, DONG Xiao-chen. Template-free synthesis of cobalt silicate nanoparticles decorated nanosheets for high performance lithium ion batteries [J]. ACS Sustainable Chemistry & Engineering, 2018, 6: 15591−15597.

[26] ZENG Jun-song, REN Yan-biao, WANG Sheng-bin, HAO Yu, WU Hao, ZHANG Shi-chao, XING Ya-lan. Hierarchical porous $ZnMn_2O_4$ microspheres assembled by nanosheets for high performance anodes of lithium ion batteries [J]. Inorganic Chemistry Frontiers, 2017, 4: 1730−1736.

[27] LI Shu-min, LI Bin, ZHONG Yao-tang, PAN Zheng-hui, XU Meng-qing, QIU Yong-cai, HUANG Qi-ming, LI Wei-shan. Mn_2O_3@C yolk-shell nanocubes as lithium-storage anode with suppressed surface electrolyte

decomposition [J]. Materials Chemistry and Physics, 2019, 222: 256−262.

[28] BHAGWAN J, KUMAR N, YADAV K L, SHARMA Y. Probing the electrical properties and energy storage performance of electrospun $ZnMn_2O_4$ nanofibers [J]. Solid State Ionics, 2018, 321: 75−82.

[29] ZHU Si-qi, CHEN Qiu-li, YANG Chao, ZHANG Yan-ru, HOU Lin-rui, PANG Gang, HE Xiang-mei, ZHANG Xiao-gang, YUAN Chang-zhou. Biomorphic template-engaged strategy towards porous zinc manganate micro-belts as a competitive anode for rechargeable lithium-ion batteries [J]. International Journal of Hydrogen Energy, 2017, 42: 14154−14165.

[30] ZHANG Ying, ZHANG Pu, XU Yue, SONG Xiao-lan, WANG Hui, MA Ting. Synthesis of pomegranate-shaped micron $ZnMn_2O_4$ with enhanced lithium storage capability [J]. Journal of Materiomics, 2021, 7: 699−707.

[31] SASIDHARACHARI K, CHO K Y, YOON S. Mesoporous $ZnMn_2O_4$ nanospheres as a nonprecious bifunctional catalyst for Zn−air batteries [J]. ACS Applied Energy Materials, 2020, 3: 3293−3301.

[32] CHEN Sheng, YAO Meng-ya, WANG Fei, WANG Juan-gang, ZHANG Yong-xing, WANG Yan-ming. Facile microemulsion synthesis of mesoporous $ZnMn_2O_4$ submicrocubes as high-rate and long-life anodes for lithium ion batteries [J]. Ceramics International, 2019, 45: 5594−5600.

[33] YANG Shu-zhen, HUANG Yan-fang, HAN Xue-chun, HAN Gui-hong. Enhancing electrochemical performance of SnO_2 anode with humic acid modification [J]. Transactions of Nonferrous Metals Society of China, 2021, 31: 2062−2073.

[34] HEIBA Z K, DEYAB M A, EI-NAGGAR A M, MOHAMED M B. Electrochemical performance of quaternary $(1-x)ZnMn_2O_4/(x)MgFe_2O_4$ solid solution as supercapacitor electrode [J]. Ceramics International, 2021, 47: 7475−7486.

[35] YANG Min, LIU Li, YAN Han-xiao, ZHANG Wen, SU Die, WEN Jia-xing, LIU Wen, YUAN Yi-ting, LIU Jun-fang, WANG Xian-you. Porous nitrogen-doped Sn/C film as free-standing anodes for lithium ion batteries [J]. Applied Surface Science, 2021, 551: 149246.

[36] ZHANG Chuan-ling, LU Bing-rong, CAO Fu-hu, YU Zhi-long, CONG Huai-ping, YU Shu-hong. Hierarchically structured Co_3O_4@carbon porous fibers derived from electrospun ZIF-67/PAN nanofibers as anodes for lithium ion batteries [J]. Journal of Materials Chemistry A, 2018, 6: 12962−12968.

[37] LI Zhen, HUANG Xiao-xiong, HU Jin-bo, STEIN A, TANG B. Synthesis and electrochemical performance of three-dimensionally ordered macroporous $CoCr_2O_4$ as an anode material for lithium ion batteries [J]. Electrochimica Acta, 2017, 247: 1−11.

[38] DUAN Jun-fei, YUAN Song, ZHU Chao, CHEN Zhao-yong, ZHANG Guan-hua, DUAN Hui-gao, LI Ling-jun, ZHU Zhi-ying. One-step synthesis of ZnO/N-doped carbon/Cu composites for high-performance lithium ion batteries anodes [J]. Synthetic Metals, 2017, 226: 39−45.

[39] CAO Hui, ZHU Si-qi, YANG Chao, BAO Rui-qi, TONG Liu-niu, HOU Lin-rui, ZHANG Xiao-gang, YUAN Chang-zhou. Metal-organic-framework-derived two-dimensional ultrathin mesoporous hetero-$ZnFe_2O_4$/ZnO nanosheets with enhanced lithium storage properties for Li-ion batteries [J]. Nanotechnology, 2016, 27: 465402.

[40] CAI Dao-ping, ZHAN Hong-bing, WANG Tai-hong. MOF-derived porous ZnO/$ZnFe_2O_4$ hybrid nanostructures as advanced anode materials for lithium ion batteries [J]. Materials Letters, 2017, 197: 241−244.

[41] XIE Qing-shui, MA Ya-ting, ZHANG Xiao-qiang, WANG Lai-sen, YUE Gaung-hui, PENG Dong-liang. ZnO/Ni/C composite hollow microspheres as anode materials for lithium ion batteries [J]. Journal of Alloys and Compounds, 2015, 619: 235−239.

[42] XIAO Li-fei, YANG Yan-yan, YIN Jia, LI Qiao, ZHANG Li-zhi. Low temperature synthesis of flower-like $ZnMn_2O_4$ superstructures with enhanced electrochemical lithium storage [J]. Journal of Power Sources, 2009, 194: 1089−1093.

[43] FENG Ting-ting, YANG Jian, DAI Si-yi, WANG Jun-chao, WU Meng-qiang. Microemulsion synthesis of $ZnMn_2O_4$/Mn_3O_4 sub-microrods for Li-ion batteries and their conversion reaction mechanism [J]. Transactions of Nonferrous Metals Society of China, 2021, 31: 265−276.

[44] GAO Qi-li, YUAN Zhao-xiao, DONG Lin-xi, WANG Gao-feng, YU Xue-bin. Reduced graphene oxide wrapped $ZnMn_2O_4$/carbon nanofibers for long-life lithium-ion batteries [J]. Electrochimica Acta, 2018, 270: 417−425.

[45] YUAN Chang-zhou, ZHANG Long-hai, HOU Lin-rui, ZHOU Lu, PANG Gang, LIAN Lin. Scalable room-temperature synthesis of mesoporous nanocrystalline $ZnMn_2O_4$ with enhanced lithium storage properties for lithium-ion batteries [J]. Chemistry, A European Journal, 2015, 21: 1262−1268.

[46] ZHANG Tong, YUE Hui-juan, QIU Hai-long, WEI Ying-jin, WANG Chun-zhong, CHEN Gang, ZHANG Dong. Nano-particle assembled porous core–shell $ZnMn_2O_4$ microspheres with superb performance for lithium batteries [J]. Nanotechnology, 2017, 28: 105403.

[47] LIU Yu-rong, BAI Jing, MA Xiao-jian, LI Jing-fa, XIONG Sheng-lin. Formation of quasi-mesocrystal $ZnMn_2O_4$ twin microspheres via an oriented attachment for lithium-ion batteries [J]. Journal of Materials Chemistry A, 2014, 2: 14236−14244.

[48] JIU Hong-fang, REN Na, ZHANG Li-xin, ZHANG Qing, GAO Yu-ying, MENG Ya-juan. Preparation and electro-chemical performance of flower-like $ZnMn_2O_4$ hollow microtubules [J]. Journal of Physics and Chemistry of Solids, 2019, 135: 109090.

[49] ZHANG Yao-hui, ZHANG Yu-wen, GUO Chun-li, TANG Bin, WANG Xiao-min, BAI Zhong-chao. Porous $ZnMn_2O_4$ nanowires as an advanced anode material for lithium ion battery [J]. Electrochimica Acta, 2015, 182: 1140−1144.

[50] ZHENG Zong-min, CHENG Yong-liang, YAN Xing-bin, WANG Ru-tao, ZHANG Peng. Enhanced electrochemical properties of graphene-wrapped $ZnMn_2O_4$ nanorods for lithium-ion batteries [J]. Journal of Materials Chemistry A, 2014, 2: 149−154.

[51] LIU Hao-wen, LE Qi. Synthesis and performance of cerium oxide as anode materials for lithium ion batteries by a chemical precipitation method [J]. Journal of Alloys and Compounds, 2016, 669: 1−7.

优化水热合成提高 $ZnMn_2O_4$ 阳极的储锂性能

蔡珂星[1,2]，罗绍华[1,2,3]，丛 君[1,2]，李 坤[1,2]，闫绳学[1,2]，侯鹏庆[2,4]，王 庆[1,2]，张亚辉[1,2]，刘 忻[1,2]

1. 东北大学 材料科学与工程学院，沈阳 110819；
2. 东北大学 秦皇岛分校 资源与材料学院 河北省介电电解质功能材料重点实验室，秦皇岛 066004；
3. 东北大学 轧制与自动化国家重点实验室，沈阳 110819；
4. 沈阳工业大学 材料科学与工程学院，沈阳 110870

摘 要：为探讨制备条件对过渡金属氧化物负极材料电化学性能的影响，以硝酸锌和硝酸锰为原料，采用水热法合成了过渡金属氧化物 $ZnMn_2O_4$ 负极材料。通过设计 4 因素 3 水平的正交试验，系统研究反应温度、反应时间、致密度、pH 值等工艺参数对合成条件的影响。X 射线衍射和扫描电镜证实 $ZnMn_2O_4$ 具有微米级块状结构及 $I4_1/amd$ 空间群。在优化的制备条件下，Li/$ZnMn_2O_4$ 电池的首次放电比容量为 933.1 mA·h/g，在 0.1C 倍率下循环 100 次后放电比容量仍为 249.3 mA·h/g。正交优化后的样品具有良好的循环性能和倍率性能。

关键词：尖晶石 $ZnMn_2O_4$ 结构；锂离子电池；电化学性能；水热反应；正交实验

(Edited by Wei-ping CHEN)